

Two-axis twisting using Floquet-engineered XYZ spin models with polar molecules

<https://doi.org/10.1038/s41586-024-07883-2>

Received: 26 April 2024

Accepted: 29 July 2024

Published online: 11 September 2024

 Check for updates

Calder Miller¹, Annette N. Carroll¹, Junyu Lin¹, Henrik Hirzler¹, Haoyang Gao², Hengyun Zhou^{2,3}, Mikhail D. Lukin² & Jun Ye¹

Polar molecules confined in an optical lattice are a versatile platform to explore spin-motion dynamics based on strong, long-range dipolar interactions^{1,2}. The precise tunability³ of Ising and spin-exchange interactions with both microwave and d.c. electric fields makes the molecular system particularly suitable for engineering complex many-body dynamics^{4–6}. Here we used Floquet engineering⁷ to realize new quantum many-body systems of polar molecules. Using a spin encoded in the two lowest rotational states of ultracold ⁴⁰K⁸⁷Rb molecules, we mutually validated XXZ spin models tuned by a Floquet microwave pulse sequence against those tuned by a d.c. electric field through observations of Ramsey contrast dynamics. This validation sets the stage for the realization of Hamiltonians inaccessible with static fields. In particular, we observed two-axis twisting⁸ mean-field dynamics, generated by a Floquet-engineered XYZ model using itinerant molecules in two-dimensional layers. In the future, Floquet-engineered Hamiltonians could generate entangled states for molecule-based precision measurement⁹ or could take advantage of the rich molecular structure for quantum simulation of multi-level systems^{10,11}.

Periodic driving of a quantum system, known as Floquet engineering, can substantially modify the symmetries and dynamics of the system, leading to new physics and applications. For example, dynamical decoupling^{12,13}, consisting of repeated spin-echo pulses, enables rejection of noise, extending coherence in quantum computing¹⁴ and metrology¹⁵ applications. By periodically modulating optical lattices, motion of atoms can be controlled¹⁶, enabling simulation of gauge theories¹⁷ and anyonic statistics¹⁸. By driving internal degrees of freedom in spin systems, time crystals^{19,20} and tunable quantum magnets^{21,22} have been created. Many other possible applications of Floquet engineering techniques are being explored, including the realization of topological insulators with ultracold molecules²³ and generation of metrologically useful Greenberger–Horne–Zeilinger-like²⁴ or spin-squeezed states²⁵.

Floquet engineering of interacting spin systems has been demonstrated in a range of physical platforms, including nuclear spins^{26–28}, superconducting qubits²⁹, Rydberg atoms^{21,30}, solid-state defects^{7,19,22,31}, trapped ions³² and ultracold molecules⁵. Optically trapped ultracold molecules^{33,34} present a unique combination of features advantageous for studying many-body physics^{1,2}. Scalable systems with tunable geometry and high-fidelity, state-resolved imaging of single particles^{5,35–38} can be realized using optical tweezers^{35,36,38–40} or lattices^{41,42}. With appropriate trapping conditions^{43–47}, disorder and particle loss can be rendered much weaker than interactions, enabling study of highly coherent many-body systems. Rich rotational and hyperfine level structures allow tuning of interactions through choice of states⁴ and simulation of higher-spin systems⁴⁸. Microwave pulses enable fast, high-fidelity state control^{4,41,49}.


In previous work⁴ using itinerant molecules, d.c. electric fields enabled tuning across a range of $U(1)$ -symmetric XXZ interactions,

ranging from pure spin-exchange to an Ising-interaction-dominated regime. However, less symmetric spin Hamiltonians exhibit rich phases and dynamics, including efficient generation of spin-squeezed states through two-axis twisting (TAT)⁸, but remain inaccessible with electric field tuning. Such systems can be explored through Floquet engineering, which can break $U(1)$ symmetry through rotation of the spins about arbitrary axes on the Bloch sphere⁷.

Despite its broad utility, Floquet engineering has not been self-consistently validated against static Hamiltonians on an experimental platform. Such benchmarking could yield insight into how experimental imperfections limit Floquet engineering schemes. Here we utilize the unique molecular level structure to validate that Floquet-engineered XXZ models produce similar Ramsey contrast decay dynamics, which probe energy shifts arising from interactions between molecules^{41,50}, to those tuned by electric field for both pinned and itinerant molecules. Our measurements reveal regimes in which Floquet engineering works well, but also settings in which its performance can be further improved. These verification protocols between different experimental implementations are important for the progress of quantum information science in general⁵¹.

Building on the comparison of XXZ spin dynamics, we designed and implemented a Floquet pulse sequence for generating TAT⁸, which can produce spin-squeezed states with Heisenberg scaling applicable to precision measurements using molecules⁹. Although TAT has been challenging to realize experimentally⁵², our molecular system with strong dipolar interactions provides a remarkably robust platform to implement this Hamiltonian through Floquet engineering. We characterized the dynamics of the Bloch vector under TAT using itinerant molecules, finding excellent agreement with a collective mean-field model.

¹JILA, National Institute of Standards and Technology and Department of Physics, University of Colorado, Boulder, CO, USA. ²Department of Physics, Harvard University, Cambridge, MA, USA.

³QuEra Computing, Boston, MA, USA. e-mail: calder.miller@colorado.edu; ye@jila.colorado.edu

Floquet spin models

The dynamics of a quantum system under periodic driving can be described with a Magnus expansion⁵³. Its leading order for small t_c/T , in which t_c is the period of the cycle and T is the characteristic timescale of interactions, is average Hamiltonian theory⁵⁴. Under average Hamiltonian theory, the system evolves under the interaction picture Hamiltonian $H_{\text{avg}} = \frac{1}{t_c} \int_0^{t_c} H(t) dt$, in which $H(t) = H(t - t_c)$ is the periodic Hamiltonian. If H consists of periods of free evolution separated by rapid changes of the Hamiltonian, $H_{\text{avg}} = \frac{1}{t_c} \sum_i \tau_i H_i$, in which τ_i is the free evolution time under Hamiltonian H_i in each cycle. In spin systems studied experimentally, this can be realized by applying rapid microwave pulses that rotate each spin by an angle θ about an axis \hat{n} on the Bloch sphere. Higher-order corrections accounting for finite t_c and pulse time can be accounted for in designing Floquet pulse sequences¹⁵.

The so-called XYZ spin models of the form $H_{\text{XYZ}} = \sum_{i<j} J_{ij} (g_x s_i^x s_j^x + g_y s_i^y s_j^y + g_z s_i^z s_j^z)$, in which i and j index the spins and J_{ij} encodes the geometric scaling of the coupling strengths \mathbf{g} , describe fundamental phenomena in magnetism³. In particular, the subspace of XXZ models with $g_x = g_y = g_{\perp}$, which can be parametrized by the anisotropy $\chi = g_z - g_{\perp}$, includes the Ising ($g_{\perp} = 0$), XY ($g_z = 0$) and Heisenberg ($\chi = 0$) models. Spins encoded in rotational levels $|0\rangle = |N=0, m_N=0\rangle$ and $|1\rangle = |1,0\rangle$ of polar molecules natively realize dipolar XXZ models with $J_{ij} \propto \frac{1-3\cos^2\theta_{ij}}{|r_{ij}|^3}$, in which θ_{ij} is the angle between the quantization axis defined by the electric field \mathbf{E} and the displacement \mathbf{r}_{ij} . N is the rotational quantum number, and m_N is its projection along the quantization axis^{4,55}. At low electric fields, $g_z \approx 0$, so the molecules predominantly interact through spin-exchange $XX + YY$ interactions. The ratio of Ising interactions g_z to spin-exchange interactions g_{\perp} can be tuned by applying a d.c. electric field that mixes rotational states, inducing a dipole moment in the laboratory frame (Fig. 1a). Microwave pulses can rotate the state on the Bloch sphere, transforming the $XX + YY$ interaction into $XX + ZZ$ or $YY + ZZ$ interactions (Fig. 1b). By choosing the ratio of times $t_{X,Y,Z}$ spent in the different frames, a range of XYZ models can be realized (shaded triangle in Fig. 1c).

Tunable XXZ Hamiltonians

Dipolar XXZ spin models have been realized in a variety of platforms, including Rydberg atoms^{21,30}, magnetic atoms⁵⁶, nitrogen vacancy centres²² and polar molecules. With molecules, bulk magnetization dynamics of the XY model in a disordered three-dimensional (3D) lattice^{41,50} were explored. Similar observations were recently made in a 2D system with a quantum gas microscope⁵, measuring the evolution of spin correlations under a Floquet pulse sequence that engineered an XXZ model at $|\mathbf{E}| = 0$. Previously, we used electric fields to tune interactions between itinerant molecules in a stack of 2D layers⁴, which at short times approximates an all-to-all spin model⁵⁷. In ref. 6, we studied electric field-tuned lattice spin models, including generalized t - J models.

Here we present a systematic study of a range of Floquet-engineered Hamiltonians, including an XYZ model for TAT. In doing so, we demonstrate the applicability of advanced pulse sequences for robust engineering of interactions and cancellation of disorder, explore the efficacy of Floquet engineering in systems involving both spin dynamics and motion, and cross-verify the Floquet engineering and electric field tuning of Hamiltonians, showing the broad utility of this approach. We first explore XXZ spin models in a 3D lattice, which can be compared to measurements in ref. 6 using electric field tuning. Our system is characterized using Ramsey spectroscopy. N_{mol} $^{40}\text{K}^{87}\text{Rb}$ molecules were produced in the rovibrational ground state $|0\rangle$. A microwave $\pi/2$ pulse on the $|0\rangle \leftrightarrow |1\rangle$ transition prepared them in the state $|+Y\rangle^{\otimes N_{\text{mol}}}$, after which they evolved for a time t , during which a microwave pulse sequence was applied, before another $\pi/2$ pulse with phase ϕ completed the Ramsey sequence. We then measured the numbers of molecules

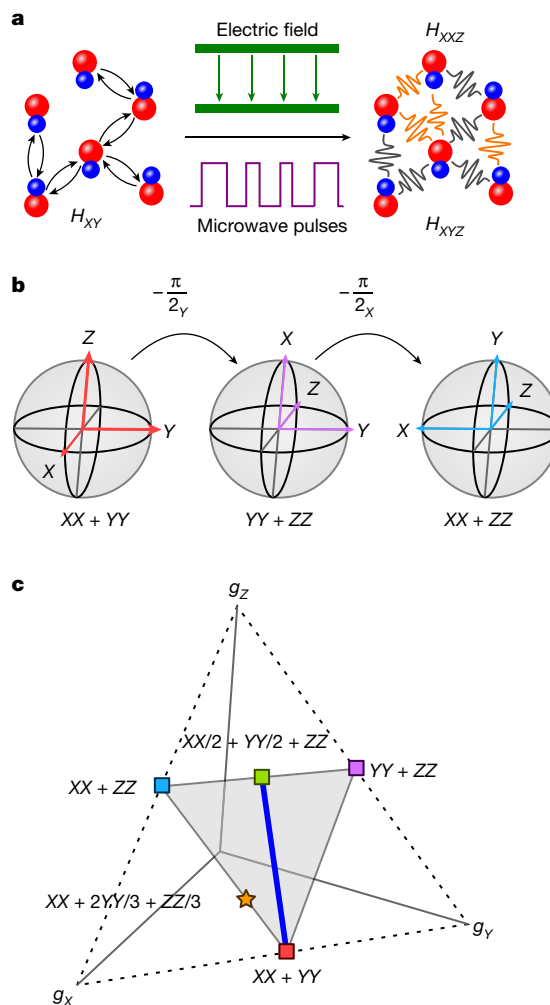


Fig. 1 | $^{40}\text{K}^{87}\text{Rb}$ Hamiltonian engineering. **a**, At low electric fields, molecules interact through spin exchange. XXZ and XY models can be realized with d.c. electric fields (green) and microwave pulse sequences (purple), respectively. **b**, Microwave $\pi/2$ pulses rotate the spins on the interaction picture Bloch sphere, transforming the spin-exchange $XX + YY$ interactions into $XX + ZZ$ or $YY + ZZ$ interactions. **c**, A range of XXZ (blue line) and XYZ (shaded triangle) interaction Hamiltonians can be realized by controlling the amount of time the spins spend in each frame, starting with the low-electric-field spin-exchange Hamiltonian between the $|0\rangle$ and $|1\rangle$ states. The orange star indicates the Hamiltonian used to study TAT dynamics. The axes represent the strength of the couplings in the XYZ Hamiltonian.

in $|0\rangle$ and $|1\rangle$ (ref. 42). The fraction of the molecules in $|1\rangle$, f_1 , was measured twice for eight values of ϕ equally spaced between 0 and 2π radians; then the Ramsey contrast was computed from the standard deviation of f_1 as in ref. 42. This process allows the length of the Bloch vector to be measured even when the phase is randomized shot to shot at longer evolution times.

To generate XXZ Hamiltonians with Floquet engineering, the molecules were produced at $|\mathbf{E}| = 1 \text{ kV cm}^{-1}$, for which the interaction Hamiltonian is predominantly spin-exchange, but for which the hyperfine and rotational structure is sufficiently split that numerous pulses on the $|0\rangle \leftrightarrow |1\rangle$ transition can be driven with only modest loss to other states. Instead of the Knill dynamical decoupling sequence¹⁴ used in ref. 6, which only removes single-particle dephasing, we used a DROID-R2D2 pulse sequence⁵⁸, which also can tune XYZ interactions, during the evolution time. We used an average pulse spacing of 100 μs , which optimizes the coherence time for an XXX model (see Methods). By varying the time in the different frames in the sequence, the

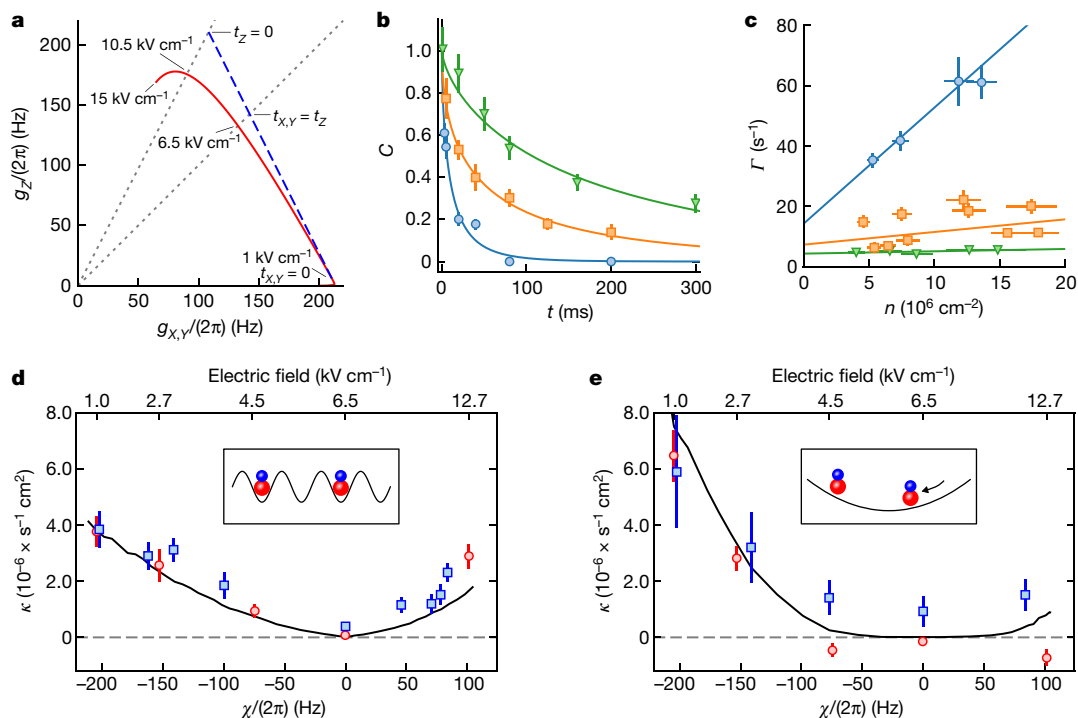


Fig. 2 | Benchmarking XXZ spin dynamics. **a**, XXZ Hamiltonians can be prepared with electric fields (red solid line) and Floquet engineering (blue dashed line). The dashed diagonal lines show the subspaces of coefficients with equal ratio g_x/g_z corresponding to the most Ising Hamiltonian that can be prepared with Floquet engineering (left) and the Heisenberg XXX model (right). **b**, Ramsey contrast as a function of time for a spin-exchange model (blue circles), a Floquet-engineered XXX model (orange squares) and an XXX model realized with electric fields (green triangles) with initial densities of about $1.6 \times 10^7 \text{ cm}^{-2}$. The lines are fits to a stretched exponential. The error bars on the data are 1 s.d. from bootstrapping. **c**, The fitted contrast decay rate plotted as a function of 2D density for a spin-exchange model (blue circles),

a Floquet-engineered XXX model (orange squares) and an XXX model realized with electric fields (green triangles). The Γ error bars are 1 s.e. from stretched exponential fits and the n error bars are 1 s.e. from the initial density of an exponential fit. **d**, The density-normalized contrast decay rate κ plotted as a function of $\chi = g_z - g_x$ and (effective, in the case of the Floquet data) electric field for simulations (black line), electric field data (red circles) and Floquet data (blue squares) for molecules pinned in a deep 3D lattice (schematic in inset). The error bars are 1 s.e. from a linear fit. **e**, Same as **d**, but for itinerant molecules in a 1D vertical lattice. The electric field-tuned data and simulations in this figure are from ref. 6.

interaction Hamiltonian can be tuned between approximately $g_{\perp,Z} = (g_{\perp}^0, 0)$ and $g_{\perp,Z} = (\frac{g_{\perp}^0}{2}, g_{\perp}^0)$ (dashed blue trace in Fig. 2a), which corresponds to $|\mathbf{E}| = 10.5 \text{ kV cm}^{-1}$. Here, g_{\perp}^0 is the native spin-exchange interaction. For comparison, in ref. 6, by varying $|\mathbf{E}|$ between 1 and 12.7 kV cm^{-1} , the coefficients $g_{\perp,Z}$ of the XXZ Hamiltonian were tuned between $2\pi \times (210, 6) \text{ Hz}$ and $2\pi \times (75, 177) \text{ Hz}$ for molecules on adjacent lattice sites in the plane perpendicular to \mathbf{E} (solid red trace in Fig. 2a).

The contrast was then measured for different t by varying the number of times the pulse sequence was repeated. The contrast decay curve is fitted with a stretched exponential model $C(t) = e^{-(t/\tau)^{\nu}}$, in which Γ is the contrast decay rate and ν is the stretching parameter describing sub-exponential decay due to number loss, spatial disorder or other effects^{6,22,59}. Sample contrast decay traces for initial densities of approximately $1.6 \times 10^7 \text{ cm}^{-2}$ are shown in Fig. 2b for spin-exchange interactions (blue circles), Floquet-engineered XXX interactions (orange squares) and XXX interactions realized with electric field (green triangles). The contrast decay is much slower for both realizations of XXX interactions than for the spin-exchange interactions. The contrast decay for the Floquet-engineered XXX interaction is slightly faster than for the electric field-tuned XXX interaction, possibly because of a slower rate of dynamical decoupling pulses or higher-order terms not fully symmetrized by the Floquet engineering.

To ensure that the measured contrast decay is due to dipolar many-body interactions and not particle loss or one-body dephasing, we measured contrast decay curves at several initial average densities n (Methods). In Fig. 2c, the fitted Γ is plotted as a function of 2D density for spin-exchange interactions (blue circles), Floquet-engineered XXX

interactions (orange squares) and XXX interactions realized with electric field (green triangles). We fit a linear model $\Gamma = \kappa n + \Gamma_0$ to the data (lines in Fig. 2c), extracting the slope κ , which describes the density dependence of contrast decay due to interactions. Linear fits to the data show a much larger κ for the spin-exchange model than the XXX model, which has minimal density dependence. The non-zero y -intercepts Γ_0 are a measure of residual single-particle dephasing (see Methods and Extended Data Fig. 5).

We equate the XXZ Hamiltonians realized by electric fields and Floquet engineering by determining the value of $|\mathbf{E}|$ that yields the same ratio of g_x to g_z as a set of Floquet timings (Fig. 2a). As the overall strength of the interaction decreases for higher electric fields but remains constant for the Floquet sequences, we rescale the Floquet data's κ by the ratio of g_x under $|\mathbf{E}|$ to its value under the Floquet Hamiltonians. We plot κ as a function of χ for both datasets (Fig. 2d). There is good agreement between their dynamics, suggesting that Floquet engineering is realizing the desired spin models. When the molecules are confined in a deep 3D lattice, we find that κ changes approximately linearly as a function of $|\chi|$, decreasing to approximately zero at the Heisenberg point where $\chi = 0$; then increasing as the Ising interactions come to dominate. This trend agrees with a moving average cluster expansion simulation⁵⁰ of the contrast decay from ref. 6.

To investigate the limitations of Floquet engineering, we applied the same pulse sequence to itinerant molecules confined in a 1D optical lattice (Fig. 2e), for which motion and collisions complicate the Hamiltonian⁶. In the spin-exchange regime in which the Floquet engineering only slightly modifies the Hamiltonian, we observe excellent agreement

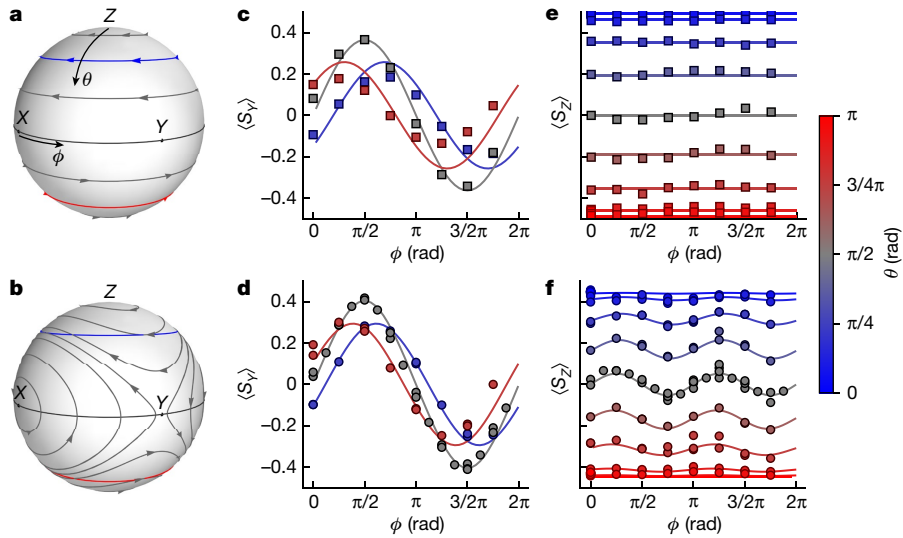


Fig. 3 | Engineering OAT and TAT. **a, b**, The Bloch vector phase portraits for OAT (**a**) and TAT (**b**) on the Bloch sphere. The blue, dark grey and red latitudinal lines mark $\theta = \frac{\pi}{4}, \frac{\pi}{2}, \frac{3\pi}{4}$ respectively. **c–f**, The projection of the average Bloch vector in the Y (**c, d**) and Z (**e, f**) directions for OAT (**c, e**) and TAT (**d, f**) as a

function of the phase (x axis) and tipping angle (colour) of the initial state after 2.4 ms evolution. The points are experimental data, and the solid lines are results from a mean-field simulation.

between the electric field-tuned and Floquet-engineered dynamics. However, in the Heisenberg and Ising regimes, the Floquet-engineered model shows a higher rate of density-dependent contrast decay than the electric field-controlled version. We expect this to occur as the contrast decay in an itinerant system is dominated by short-range collisions between molecules⁵, which was modelled in ref. 6 by a Monte Carlo simulation (solid line in Fig. 2e) incorporating two-particle scattering. The collisions take place over durations comparable to the Floquet pulse spacing and have scattering properties set by the electric field. Nevertheless, a similar overall trend is observed with Floquet engineering, indicating that control is still possible over itinerant models.

Realizing TAT

Beyond providing an alternative to electric field tuning to realize XXZ models, Floquet pulse sequences can engineer general XYZ models, which are inaccessible using only d.c. electric fields because the energy conservation under a strong quantization axis enforces $U(1)$ symmetry on the form of the native interaction. One special case, with $g_x = -g_z$, $g_y = 0$, generates TAT dynamics. TAT can achieve spin squeezing with number scaling reaching the Heisenberg limit, exceeding the performance of one-axis twisting (OAT) generated by XXZ Hamiltonians^{8,60}. Generation of spin-squeezed states with ultracold molecules could enhance applications in precision metrology, including detection of beyond-standard-model physics⁹. However, despite several proposals^{25,60}, TAT mean-field dynamics have only recently been observed in a cavity quantum electrodynamics system⁵², as the required XYZ Hamiltonians are not native to common platforms.

Ultracold molecules in a 1D optical lattice provide a platform with sufficient control to study TAT. We implemented TAT and observed the evolution of Bloch vectors under the Hamiltonian by Floquet engineering the interactions between itinerant molecules in 2D layers, which approximate all-to-all interactions^{4,57}. The native spin-exchange interactions generate OAT about the Z axis (Fig. 3c) plus an isotropic XXX interaction, with Hamiltonian $H_{\text{OAT}} = g_{\perp} \sum_{i<j} J_{ij} (\mathbf{s}_i \cdot \mathbf{s}_j - s_i^z s_j^z)$. The Hamiltonian is invariant under dynamical decoupling sequences consisting solely of π pulses such as XY8 (Extended Data Fig. 1a). As rotations on the Bloch sphere preserve the trace $g_x + g_y + g_z$ of the interaction Hamiltonian, the native low-field Hamiltonian $g_{\perp} > 0$, $g_z \approx 0$ cannot be transformed into pure TAT. Instead, we realize the

Hamiltonian $H_{\text{TAT}} = g_{\perp} \sum_{i<j} J_{ij} \left(\frac{2}{3} \mathbf{s}_i \cdot \mathbf{s}_j + \frac{1}{3} (s_i^x s_j^x - s_i^z s_j^z) \right)$, as proposed in ref. 25. As any point on the surface of the Bloch sphere is an eigenstate of the $\mathbf{s}_i \cdot \mathbf{s}_j$ term in H_{OAT} and H_{TAT} , the term does not affect the short-time dynamics. To engineer TAT while cancelling inhomogeneous disorder, we used a modified XY8 pulse sequence, XY8-TAT (Extended Data Fig. 1b), in which the π pulses about the Y axis are split into pairs of $\pi/2$ pulses. For pulse spacing τ , this results in 4τ being spent with $XX + ZZ$ interactions and 8τ with $XX + YY$ interactions, realizing H_{TAT} on average (see Methods).

We first prepared the spins in $|0\rangle$ and applied a pulse with area θ about axis $-\sin\phi X + \cos\phi Y$ on the Bloch sphere, giving an initial average Bloch vector $\langle \mathbf{S}_0 \rangle = \frac{1}{2} (\cos\phi \sin\theta, \sin\phi \sin\theta, \cos\theta)$. We then repeated either XY8-TAT or a standard XY8 pulse sequence for 2.4 ms before measuring the collective Bloch vector in the X , Y or Z bases. This measurement requires excellent shot-to-shot phase coherence, so we operated at $|E| = 0$ to reduce fluctuations in the transition frequency from electric field noise. The data are compared to a mean-field, all-to-all simulation of the dynamics (Methods) for which the interaction strength and dephasing rate are fitted to the data.

OAT has two stable fixed points at the $\pm Z$ poles of the Bloch sphere. Between the poles, interactions rotate the Bloch vector about the Z axis (Fig. 3a). As observed in previous work⁴, the phase shift $\Delta\phi = \arctan \frac{\langle S_y^Y \rangle}{\langle S_x^X \rangle} - \arctan \frac{\langle S_y^0 \rangle}{\langle S_x^0 \rangle}$ under OAT is proportional to $\langle S_0^Z \rangle$ (Fig. 3c). We also see that $\langle S^Z \rangle$ does not depend on ϕ (Fig. 3e). By contrast, TAT has two unstable fixed points at the $\pm Y$ poles of the Bloch sphere and four stable fixed points at the $\pm X$ and $\pm Z$ poles^{61,62}. Between the fixed points, the Bloch vector moves alternately upwards and downwards as a function of angle in the X - Z plane, completing two oscillations around the circumference of the sphere (Fig. 3b). This behaviour is apparent in our data (Fig. 3f).

TAT can prepare spin-squeezed states from initial coherent states at the poles of the Bloch sphere by compressing and extending the quasiprobability distribution in orthogonal directions rotated by $\pi/4$ radians relative to the twisting axes⁶¹ (Fig. 4a). We observed the mean-field version of these dynamics by preparing a ring of initial states in an X - Z plane of the Bloch sphere for different values of $\langle S_0^Y \rangle$ and fitting their positions after evolution under TAT for 2.4 ms to an ellipse (positions before (after) evolution in blue (orange) are shown in insets in Fig. 4b). We plot the ratio of the sizes of the fitted ellipses along the $X = \pm Z$ directions as a function of $\langle S_0^Y \rangle$ (Fig. 4b). Near $\langle S_0^Y \rangle = \pm 0.5$,

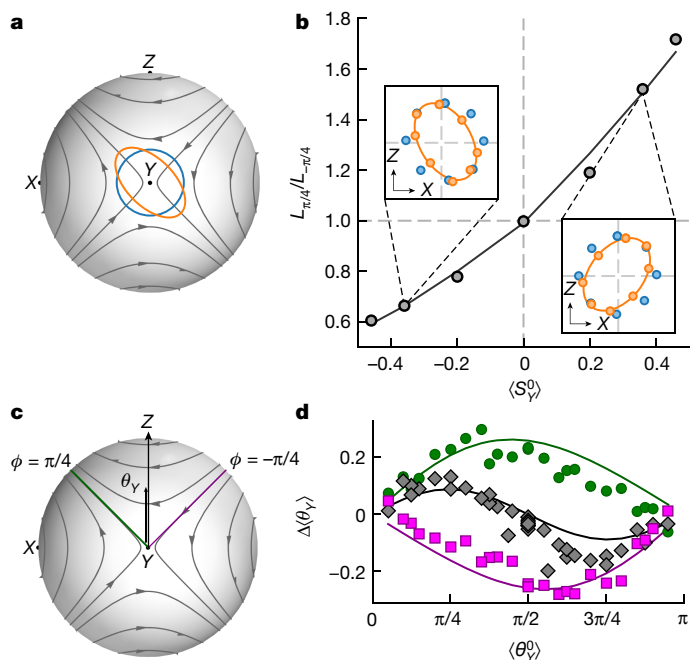


Fig. 4 | TAT mean-field dynamics. **a**, TAT mean-field dynamics plotted around the +Y pole of the Bloch sphere, where spin squeezing would be generated. In a mean-field analogue to squeezing, points along the blue circle evolve to points along the orange ellipse. Similar dynamics mirrored about the Y–Z plane would be observed near the –Y pole. **b**, An ellipse is fitted to data (orange points in insets) prepared at different phases ϕ in the X–Z plane and angles θ_Y^0 from the +Y axis (blue points in insets) after 2.4 ms evolution time. The aspect ratio of the ellipse, as measured along axes with angle $\frac{\pi}{4}$ and $-\frac{\pi}{4}$ from the +Z axis, is plotted as a function of the initial spin $\langle S_Y^0 \rangle = \frac{\cos\theta_Y^0}{2}$ (black points). The same fit to the mean-field simulations is plotted as the black line. The insets show the X and Z components of the initial and final Bloch vectors for $\theta_Y^0 = \pi/4$ and $3\pi/4$. The axis range is –0.5 to 0.5. **c**, TAT mean-field dynamics plotted around the +Y pole of the Bloch sphere. The contours at $\phi = -\frac{\pi}{4}, 0$ and $\frac{\pi}{4}$ are plotted in green, dark grey and purple, respectively. **d**, Measured values of $\langle \theta_Y \rangle$ after 2.4 ms evolution under TAT dynamics are plotted as a function of θ_Y^0 for $\phi = \frac{\pi}{4}$ (green circles), 0 (grey diamonds) and $-\frac{\pi}{4}$ (purple squares). The lines are mean-field simulation results under the same conditions.

the ellipses are more stretched, with the major axis in opposite directions. The measured shapes agree well with a mean-field simulation of the experiment (solid line in Fig. 4d). The reduced size of the ellipse after time evolution relative to the initial circle is probably a result of dephasing from collisions and inhomogeneous dynamics between the layers.

Near the $\pm Y$ poles, the rate of rotation of the Bloch vector is proportional to the Bloch vector’s angle from the pole, resulting in exponential growth of the displacement with time. We measured the change in the angle θ_Y between $\langle \mathbf{S} \rangle$ and the Y axis for an evolution time of 2.4 ms after preparing states at a range of $\langle S_Y^0 \rangle$ values for $\langle S_X^0 \rangle = \pm \langle S_Z^0 \rangle$, for which $\frac{d\theta_Y}{dt}$ should be extremized, and $\langle S_X^0 \rangle = 0$, for which it should be zero (green, purple and grey lines in Fig. 4c, respectively). We observe good agreement with the mean-field model at 2.4 ms evolution time (green ($\langle S_X^0 \rangle = \langle S_Z^0 \rangle$), purple ($\langle S_X^0 \rangle = -\langle S_Z^0 \rangle$) and grey ($\langle S_X^0 \rangle = 0$) points and solid lines in Fig. 4d). As a result of the finite time, $\Delta\theta_Y$ (grey points in Fig. 4d) is non-zero for $\langle S_X^0 \rangle = 0$, although the $\frac{d\theta_Y}{dt} = 0$ at $t = 0$.

Outlook

In this work, we systematically characterize Floquet engineering methods for controlling interactions between ultracold molecules and demonstrate their application to realizing spin Hamiltonians applicable to metrology and many-body physics. Comparing Ramsey

contrast dynamics produced by Floquet engineering against those generated by a d.c. electric field helps verify its efficacy. Now that their performance has been demonstrated, these Hamiltonian engineering tools will enable diverse future research. If an interacting ensemble was prepared in a single layer of an optical lattice and detection efficiency was improved, it should be possible to verify entanglement of a spin-squeezed state prepared through OAT or TAT using noise measurements⁶³. Time-reversal of the dynamics^{64,65}, implemented using another rotational level⁴, may enable quantum-enhanced sensing with relaxed detection requirements. The rich level structure of molecules will also enable investigation of dynamics of higher spins, for which similar Hamiltonian engineering techniques¹¹ exist, and exploration of synthetic dimensions encoded in rotational states¹⁰.

Online content

Any methods, additional references, Nature Portfolio reporting summaries, source data, extended data, supplementary information, acknowledgements, peer review information; details of author contributions and competing interests; and statements of data and code availability are available at <https://doi.org/10.1038/s41586-024-07883-2>.

- Langen, T., Valtolina, G., Wang, D. & Ye, J. Quantum state manipulation and science of ultracold molecules. *Nat. Phys.* **20**, 702–712 (2024).
- Cornish, S. L., Tarbutt, M. R. & Hazzard, K. R. A. Quantum computation and quantum simulation with ultracold molecules. *Nat. Phys.* **20**, 730–740 (2024).
- Gorshkov, A. V. et al. Tunable superfluidity and quantum magnetism with ultracold polar molecules. *Phys. Rev. Lett.* **107**, 115301 (2011).
- Li, J.-R. et al. Tunable itinerant spin dynamics with polar molecules. *Nature* **614**, 70–74 (2023).
- Christakis, L. et al. Probing site-resolved correlations in a spin system of ultracold molecules. *Nature* **614**, 64–69 (2023).
- Carroll, A. N. et al. Observation of coherent generalized t-J spin dynamics with tunable dipolar interactions. Preprint at <https://doi.org/10.48550/arXiv.2404.18916> (2024).
- Choi, J. et al. Robust dynamic Hamiltonian engineering of many-body spin systems. *Phys. Rev. X* **10**, 031002 (2020).
- Kitagawa, M. & Ueda, M. Squeezed spin states. *Phys. Rev. A* **47**, 5138–5143 (1993).
- Safronova, M. S. et al. Search for new physics with atoms and molecules. *Rev. Mod. Phys.* **90**, 025008 (2018).
- Sundar, B., Gadway, B. & Hazzard, K. R. A. Synthetic dimensions in ultracold polar molecules. *Sci. Rep.* **8**, 3422 (2018).
- Zhou, H. et al. Robust Hamiltonian Engineering for Interacting Qudit Systems. *Phys. Rev. X* **14**, 031017 (2024).
- Viola, L. & Lloyd, S. Dynamical suppression of decoherence in two-state quantum systems. *Phys. Rev. A* **58**, 2733–2744 (1998).
- Viola, L., Knill, E. & Lloyd, S. Dynamical decoupling of open quantum systems. *Phys. Rev. Lett.* **82**, 2417–2421 (1999).
- Souza, A. M., Álvarez, G. A. & Suter, D. Robust dynamical decoupling for quantum computing and quantum memory. *Phys. Rev. Lett.* **106**, 240501 (2011).
- Zhou, H. et al. Robust higher-order Hamiltonian engineering for quantum sensing with strongly interacting systems. *Phys. Rev. Lett.* **131**, 220803 (2023).
- Weitenberg, C. & Simonet, J. Tailoring quantum gases by Floquet engineering. *Nat. Phys.* **17**, 1342–1348 (2021).
- Aidelsburger, M. et al. Realization of the Hofstadter Hamiltonian with ultracold atoms in optical lattices. *Phys. Rev. Lett.* **111**, 185301 (2013).
- Kwan, J. et al. Realization of 1D anyons with arbitrary statistical phase. Preprint at <https://doi.org/10.48550/arxiv.2306.01737> (2023).
- Choi, S. et al. Observation of discrete time-crystalline order in a disordered dipolar many-body system. *Nature* **543**, 221–225 (2017).
- Zhang, J. et al. Observation of a discrete time crystal. *Nature* **543**, 217–220 (2017).
- Geier, S. et al. Floquet Hamiltonian engineering of an isolated many-body spin system. *Science* **374**, 1149–1152 (2021).
- Martin, L. S. et al. Controlling local thermalization dynamics in a Floquet-engineered dipolar ensemble. *Phys. Rev. Lett.* **130**, 210403 (2023).
- Schuster, T. et al. Floquet engineering ultracold polar molecules to simulate topological insulators. *Phys. Rev. A* **103**, 063322 (2021).
- Zhang, X., Hu, Z. & Liu, Y.-C. Fast generation of GHZ-like states using collective-spin XYZ model. *Phys. Rev. Lett.* **132**, 113402 (2024).
- Liu, Y. C., Xu, Z. F., Jin, G. R. & You, L. Spin squeezing: transforming one-axis twisting into two-axis twisting. *Phys. Rev. Lett.* **107**, 013601 (2011).
- Carr, H. Y. & Purcell, E. M. Effects of diffusion on free precession in nuclear magnetic resonance experiments. *Phys. Rev.* **94**, 630–638 (1954).
- Waugh, J. S., Huber, L. M. & Haeblerlen, U. Approach to high-resolution NMR in solids. *Phys. Rev. Lett.* **20**, 180–182 (1968).
- Peng, P., Yin, C., Huang, X., Ramanathan, C. & Cappellaro, P. Floquet prethermalization in dipolar spin chains. *Nat. Phys.* **17**, 444–447 (2021).
- Nguyen, L. B. et al. Programmable Heisenberg interactions between Floquet qubits. *Nat. Phys.* <https://doi.org/10.1038/s41586-023-02326-7> (2024).

30. Scholl, P. et al. Microwave engineering of programmable XXZ Hamiltonians in arrays of Rydberg atoms. *PRX Quantum* **3**, 020303 (2022).
31. Zu, C. et al. Emergent hydrodynamics in a strongly interacting dipolar spin ensemble. *Nature* **597**, 45–50 (2021).
32. Morong, W. et al. Engineering dynamically decoupled quantum simulations with trapped ions. *PRX Quantum* **4**, 010334 (2023).
33. Chotia, A. et al. Long-lived dipolar molecules and Feshbach molecules in a 3D optical lattice. *Phys. Rev. Lett.* **108**, 080405 (2012).
34. Moses, S. A. et al. Creation of a low-entropy quantum gas of polar molecules in an optical lattice. *Science* **350**, 659–662 (2015).
35. Picard, L. R. B., Patenotte, G. E., Park, A. J., Gebretsadkan, S. F. & Ni, K.-K. Site-selective preparation and multi-state readout of molecules in optical tweezers. *PRX Quantum* **5**, 020344 (2024).
36. Ruttley, D. K., Guttridge, A., Hepworth, T. R. & Cornish, S. L. Enhanced quantum control of individual ultracold molecules using optical tweezer arrays. *PRX Quantum* **5**, 020333 (2024).
37. Bao, Y. et al. Dipolar spin-exchange and entanglement between molecules in an optical tweezer array. *Science* **382**, 1138–1143 (2023).
38. Holland, C. M., Lu, Y. & Cheuk, L. W. On-demand entanglement of molecules in a reconfigurable optical tweezer array. *Science* <https://doi.org/10.1126/science.adf4272> (2023).
39. Anderegg, L. et al. An optical tweezer array of ultracold molecules. *Science* **365**, 1156–1158 (2019).
40. Kaufman, A. M. & Ni, K.-K. Quantum science with optical tweezer arrays of ultracold atoms and molecules. *Nat. Phys.* **17**, 1324–1333 (2021).
41. Yan, B. et al. Observation of dipolar spin-exchange interactions with lattice-confined polar molecules. *Nature* **501**, 521–525 (2013).
42. Tobias, W. G. et al. Reactions between layer-resolved molecules mediated by dipolar spin exchange. *Science* **375**, 1299–1303 (2022).
43. Neyenhuis, B. et al. Anisotropic polarizability of ultracold polar $^{40}\text{K}^{87}\text{Rb}$ molecules. *Phys. Rev. Lett.* **109**, 230403 (2012).
44. Seeßelberg, F. et al. Extending rotational coherence of interacting polar molecules in a spin-decoupled magic trap. *Phys. Rev. Lett.* **121**, 253401 (2018).
45. Park, A. J. et al. Extended rotational coherence of polar molecules in an elliptically polarized trap. *Phys. Rev. Lett.* **131**, 183401 (2023).
46. Burchesky, S. et al. Rotational coherence times of polar molecules in optical tweezers. *Phys. Rev. Lett.* **127**, 123202 (2021).
47. Gregory, P. D. et al. Second-scale rotational coherence and dipolar interactions in a gas of ultracold polar molecules. *Nat. Phys.* <https://doi.org/10.1038/s41567-023-02328-5> (2024).
48. Brennen, G. K., Micheli, A. & Zoller, P. Designing spin-1 lattice models using polar molecules. *New J. Phys.* **9**, 138 (2007).
49. Ospelkaus, S. et al. Controlling the hyperfine state of Rovibronic ground-state polar molecules. *Phys. Rev. Lett.* **104**, 030402 (2010).
50. Hazzard, K. R. A. et al. Many-body dynamics of dipolar molecules in an optical lattice. *Phys. Rev. Lett.* **113**, 195302 (2014).
51. Altman, E. et al. Quantum simulators: architectures and opportunities. *PRX Quantum* **2**, 017003 (2021).
52. Luo, C. et al. Hamiltonian engineering of collective XYZ spin models in an optical cavity: from one-axis twisting to two-axis counter twisting models. Preprint at <https://doi.org/10.48550/arxiv.2402.19429> (2024).
53. Vandersypen, L. M. K. & Chuang, I. L. NMR techniques for quantum control and computation. *Rev. Mod. Phys.* **76**, 1037–1069 (2005).
54. Haeberlen, U. & Waugh, J. S. Coherent averaging effects in magnetic resonance. *Phys. Rev.* **175**, 453–467 (1968).
55. Gorshkov, A. V. et al. Quantum magnetism with polar alkali-metal dimers. *Phys. Rev. A* **84**, 033619 (2011).
56. de Paz, A. et al. Nonequilibrium quantum magnetism in a dipolar lattice gas. *Phys. Rev. Lett.* **111**, 185305 (2013).
57. Bilitewski, T. et al. Dynamical generation of spin squeezing in ultracold dipolar molecules. *Phys. Rev. Lett.* **126**, 113401 (2021).
58. Tyler, M., Zhou, H., Martin, L. S., Leita, N. & Lukin, M. D. Higher-order methods for Hamiltonian engineering pulse sequence design. *Phys. Rev. A* **108**, 062602 (2023).
59. Signoles, A. et al. Glassy dynamics in a disordered Heisenberg quantum spin system. *Phys. Rev. X* **11**, 011011 (2021).
60. Borregaard, J., Davis, E. J., Bentsen, G. S., Schleier-Smith, M. H. & Sørensen, A. S. One- and two-axis squeezing of atomic ensembles in optical cavities. *New J. Phys.* **19**, 093021 (2017).
61. Kajtoch, D. & Witkowska, E. Quantum dynamics generated by the two-axis counter-twisting Hamiltonian. *Phys. Rev. A* **92**, 013623 (2015).
62. Muñoz-Arias, M. H., Deutsch, I. H. & Poggi, P. M. Phase-space geometry and optimal state preparation in quantum metrology with collective spins. *PRX Quantum* **4**, 020314 (2023).
63. Hald, J., Sørensen, J. L., Schori, C. & Polzik, E. S. Spin squeezed atoms: a macroscopic entangled ensemble created by light. *Phys. Rev. Lett.* **83**, 1319–1322 (1999).
64. Geier, S. et al. Time-reversal in a dipolar quantum many-body spin system. Preprint at <https://doi.org/10.48550/arxiv.2402.13873> (2024).
65. Davis, E., Bentsen, G. & Schleier-Smith, M. Approaching the Heisenberg limit without single-particle detection. *Phys. Rev. Lett.* **116**, 053601 (2016).

Publisher's note Springer Nature remains neutral with regard to jurisdictional claims in published maps and institutional affiliations.

Springer Nature or its licensor (e.g. a society or other partner) holds exclusive rights to this article under a publishing agreement with the author(s) or other rightsholder(s); author self-archiving of the accepted manuscript version of this article is solely governed by the terms of such publishing agreement and applicable law.

© The Author(s), under exclusive licence to Springer Nature Limited 2024

Molecule production

We produced fermionic $^{40}\text{K}^{87}\text{Rb}$ molecules from quantum degenerate gases of potassium and rubidium by magnetoassociation followed by stimulated Raman adiabatic passage (STIRAP) to the rovibrational ground state^{34,66,67}. The molecules were produced in a 3D lattice formed from 1,064-nm light with a spacing of $a_{x,y,z} = (532, 540, 532)$ nm, in which y is the direction of gravity and our d.c. electric and magnetic fields. Owing to harmonic confinement from the lattice and an additional crossed dipole trap, the positions of the molecules approximated a Gaussian distribution with a standard deviation of $\sigma_{x,y,z} \approx (16, 2.8, 20)$ μm . The vertical extent of the distribution was measured to be $L = \frac{N_{\text{mol}}^2}{\sum_k N_k^2} = 18.5(10)$ layers with layer-resolved gradient spectroscopy⁴². Here, N_{mol} is the total molecule number and N_k is the number of molecules in the k th layer.

For the XXZ contrast decay measurements, around 12,000 molecules were created in a lattice of depth $U_{x,y,z} = (25, 65, 25)E_r$, in which E_r is the recoil energy, yielding a maximum average filling fraction of about 13%. Following STIRAP, the lattice was ramped to $U_{x,y,z} = (65, 65, 65)E_r$ in 5 ms to suppress tunnelling in the x - z plane for the pinned measurements or $U_{x,y,z} = (0, 65, 0)E_r$ for the itinerant measurements. For the OAT and TAT measurements, we used a vertical lattice of depth $40E_r$, the shallower vertical lattice resulting in lower temperature and reduced a.c. Stark shifts from the lattice's non-magic polarization^{42,43}. About 10,000 molecules were produced in 2D layers at a temperature of 158(10) nK. For all measurements, the molecules were made and imaged at the target electric field, with the frequencies of the STIRAP lasers tuned to remain resonant with the molecular transitions.

To prepare systems at different densities, we used a microwave pulse with area θ to shelve a fraction of the molecules in $|1\rangle$ while removing the molecules in $|0\rangle$ using a pulse of resonant light from the STIRAP down leg⁴. This procedure reduced the density by a factor of $\sin^2\theta/2$.

Microwave control of rotational states

We encoded a spin-1/2 system in the rotational states $|0\rangle = |N=0, m_N=0, m_K=-4, m_{\text{Rb}}=1/2\rangle$ and $|1\rangle = |N=1, m_N=0, m_K=-4, m_{\text{Rb}}=1/2\rangle$. The frequency of the $|0\rangle \leftrightarrow |1\rangle$ transition varies between 2.228 GHz at zero electric field and 4.225 GHz at $|\mathbf{E}| = 12.7$ kV cm^{-1} . We generated microwaves to drive Rabi oscillations between $|0\rangle$ and $|1\rangle$ using a custom radiofrequency synthesizer based on a field-programmable gate array whose output was mixed with a microwave local oscillator. The microwaves were bandpass-filtered, amplified and then coupled to the molecules through the in-vacuum electrodes using a bias tee. We used rectangular pulses with Rabi frequency $\Omega \approx 2\pi \times 100$ kHz except at $|\mathbf{E}| = 0$ kV cm^{-1} , at which we reduced Ω to $2\pi \times 50$ kHz to suppress off-resonant driving to other rotational and hyperfine states.

To reduce inhomogeneous broadening, we used magic-angle optical traps for the crossed dipole trap and the two horizontal lattices^{42,43}. Owing to geometric constraints, the vertical lattice was not magic.

We characterized the fidelity of our microwave pulses using the one-qubit randomized benchmarking sequence described in ref. 68. At 1 kV cm^{-1} , we measured fidelities of 0.99941(9) per $\pi/2$ pulse with itinerant molecules confined by a $65E_r$ vertical lattice and 0.99915(14) with molecules pinned in a $65E_r$ 3D lattice. At 0 kV cm^{-1} , we measured a lower fidelity of 0.9941(9) with itinerant molecules, which we attribute to off-resonant driving of other nearby hyperfine states.

A substantial fraction of the molecules are lost during the application of hundreds or thousands of microwave pulses, particularly at 0 kV cm^{-1} . As we image both $|0\rangle$ and $|1\rangle$, we can reject the effect of these erasure errors⁶⁹. During our TAT pulse sequence, the number decays with an exponential time constant of 11.2(6) ms (Extended Data Fig. 4), which is long compared to the 2.4 ms measurement time.

Optimizing Floquet timing

To optimize the pulse spacing for the Floquet XXZ data, we measured the contrast decay rate for an XXX Hamiltonian with pinned molecules, realized with a variety of pulse spacings between 25 and 400 μs (Extended Data Fig. 3). If the pulse spacing is too long, interactions between the molecules will not be well symmetrized and dephasing from inhomogeneous single-particle noise will not be effectively cancelled. If the pulse spacing is too short, pulse errors can accumulate more quickly and more molecules will be driven into other hyperfine states, causing increased loss. We therefore used a pulse spacing of 100 μs for the Floquet XXZ and XYZ Hamiltonians, which was the longest spacing that shows near-optimal contrast decay rates. For the Knill dynamical decoupling pulse sequence in ref. 6, we used a 50- μs pulse spacing, as the molecules are more sensitive to fluctuating electric fields as the dipole moment increases at larger fields, so faster dynamical decoupling improves contrast.

Extended Data Fig. 5 shows the single-particle contrast decay rate Γ_0 as a function of χ controlled by electric field (red circles) or Floquet timing (blue squares). For pinned molecules (Extended Data Fig. 5a), Γ_0 depends weakly on χ for both Floquet and electric field data. However, for itinerant molecules (Extended Data Fig. 5b), Γ_0 shows opposite trends for the two datasets. As electric field is increased, Γ_0 increases, possibly because molecules with larger induced dipole moments at larger electric fields experience larger phase shifts as they move through residual electric field gradients. For the Floquet data, Γ_0 increases as the Hamiltonian is tuned farther from the Heisenberg point $t_x = t_y = t_z$. This occurs because some of the spin-echo pulses in the DROID-R2D2 occur at longer intervals (up to 298 μs in the most spin-exchange-dominated case) such that noise from motion in electric field or optical potential gradients is less effectively cancelled. The coherence time could be improved with a different pulse sequence with shorter maximum intervals between spin-echo pulses.

Imaging and image analysis

We imaged both the $|0\rangle$ and $|1\rangle$ states of the molecules using state-selective STIRAP^{4,42}. At all electric fields used except 1 kV cm^{-1} , we transferred the population in $|0\rangle$ to the Feshbach state, and then detected the potassium atoms in the Feshbach molecules by absorption imaging. The reported number derives from a 2D Gaussian fit to the in situ distribution of the atoms. We then applied a π pulse to transfer the molecules in $|1\rangle$ to $|0\rangle$ and repeated the STIRAP and absorption imaging. At 1 kV cm^{-1} , the STIRAP depletes the molecules in $|1\rangle$, so we shelved the population in $|1\rangle$ to $|N=2, m_N=0\rangle$ during the first STIRAP. To calibrate the STIRAP efficiency, we carried out repeated STIRAP transfers between the Feshbach state and $|0\rangle$ and fitted an exponential decay to the molecule number. The one-way STIRAP efficiency is approximately 90% at 0 kV cm^{-1} , 85% at 1 kV cm^{-1} and as low as 70% at 12.7 kV cm^{-1} , and the efficiency of imaging Feshbach molecules is approximately 70% (ref. 67). Both efficiencies are factored into the reported molecule numbers and densities. The reported 2D densities are computed assuming the average molecule number in a layer $N_{2\text{D}} = N_{\text{mol}}/L$ and a Gaussian distribution with the fitted size from in situ images.

We also characterized systematic errors introduced during the imaging process by preparing a superposition $\cos\theta|0\rangle + \sin\theta|1\rangle$ with a microwave pulse immediately before our imaging sequence. For itinerant molecules, we find that for θ close to 0 or π , fewer molecules are in the minority state than would be expected from the state preparation. We attribute this to loss from inelastic collisions between the Ramsey sequence and imaging. As these collisions occur nearly 100 times more rapidly for distinguishable molecules⁴², their effect on the density can be modelled as $\frac{dn_i}{dt} \propto -\beta_p n_i n_j$ for $i \neq j$ in which the indices are over the

states $|0\rangle$ and $|1\rangle$ and β_p is the p -wave loss rate. By fitting the solution to this system of differential equations to the measured molecule numbers, we correct the density and spin data for this loss process (Extended Data Fig. 2).

Mean-field OAT and TAT models

Per the Ehrenfest theorem⁷⁰, the expectation values of the collective Bloch vector \mathbf{S} under the all-to-all Hamiltonian $H_{XYZ} = \sum_i g_i S_i^2$ evolve as $\frac{d\langle S_i \rangle}{dt} = 2 \sum_{j,k} \epsilon_{ijk} g_j \langle S_j \rangle \langle S_k \rangle$ in which $i, j, k \in \{\hat{X}, \hat{Y}, \hat{Z}\}$. We also include dephasing with rate γ^\perp , adding a term $-\gamma^\perp \langle S_i \rangle$ to the equations for $\frac{d\langle S_X \rangle}{dt}$ and $\frac{d\langle S_Y \rangle}{dt}$. We numerically solve the equations of motion to obtain final values for $\langle S_i \rangle$.

For OAT, $g_{X,Y,Z} = (g, g, 0)$ and for TAT, $g_{X,Y,Z} = (3g, 2g, g)/3$ under average Hamiltonian theory. When γ^\perp is set to zero, we observe excellent agreement between simulations using the average Hamiltonian theory interaction strengths and simulations of applying the XY8-TAT pulse sequence with XY interactions. To properly simulate the dephasing, which is partially transformed into depolarization by the Floquet pulse sequence, we chose to model the TAT dynamics by modelling the application of the XY8-TAT pulse sequence with instantaneous pulses and XY interactions between pulses.

To find the values of g and γ , we fitted the output of our simulations to the OAT and TAT data. To ensure that the fit is not dominated by points with abnormal molecule number, we included only measurements for which the number is within two standard deviations of the average number for the TAT data. We found that the sum of squares of the errors was minimized when $g = 360 \text{ s}^{-1}$ and $\gamma^\perp = 130 \text{ s}^{-1}$ for our typical molecule density of $1.08(9) \times 10^7 \text{ cm}^{-2}$.

Data availability

Data are available from the corresponding authors upon request.

Code availability

Code is available from the corresponding authors upon request.

66. Ni, K.-K. et al. A high phase-space-density gas of polar molecules. *Science* **322**, 231–235 (2008).
67. De Marco, L. et al. A degenerate Fermi gas of polar molecules. *Science* **363**, 853–856 (2019).
68. Knill, E. et al. Randomized benchmarking of quantum gates. *Phys. Rev. A* **77**, 012307 (2008).
69. Wu, Y., Kolkowitz, S., Puri, S. & Thompson, J. D. Erasure conversion for fault-tolerant quantum computing in alkaline earth Rydberg atom arrays. *Nat. Commun.* **13**, 4657 (2022).
70. Griffiths, D. J. *Introduction to Quantum Mechanics* (Cambridge Univ. Press, 2017).

Acknowledgements We thank N. Leitao, L. S. Martin and A. M. Rey for helpful discussions; K. P. ZamarSKI and F. Vietmeyer for technical contributions; and K. Kim and C. Luo for their comments on the manuscript. The work at JILA and Harvard was jointly supported by the US Department of Energy, Office of Science, National Quantum Information Science Research Centers, Quantum Systems Accelerator. Support is also acknowledged from the National Science Foundation (NSF) Quantum Leap Challenge Institutes (OMA-2016244), the NSF Physics Frontiers Centers (PHY-2317149), the Air Force Office of Scientific Research Multidisciplinary University Research Initiative, the Army Research Office Multidisciplinary University Research Initiative and the National Institute of Standards and Technology. H.G., H.Z. and M.D.L. acknowledge support from the Center for Ultracold Atoms, an NSF Physics Frontiers Center (PHY-2317134) and the NSF (PHY-2012023). C.M. acknowledges support from the Department of Defense through the National Defense Science and Engineering Graduate Fellowship. A.N.C. acknowledges support from the NSF Graduate Research Fellowship Program under grant number DGE 2040434.

Author contributions C.M., A.N.C., J.L., H.H. and J.Y. carried out the experiments and analysed the data. H.G., H.Z. and M.D.L. contributed ideas and methods for Floquet engineering. All authors discussed the results and contributed to the manuscript.

Competing interests The authors declare no competing interests.

Additional information

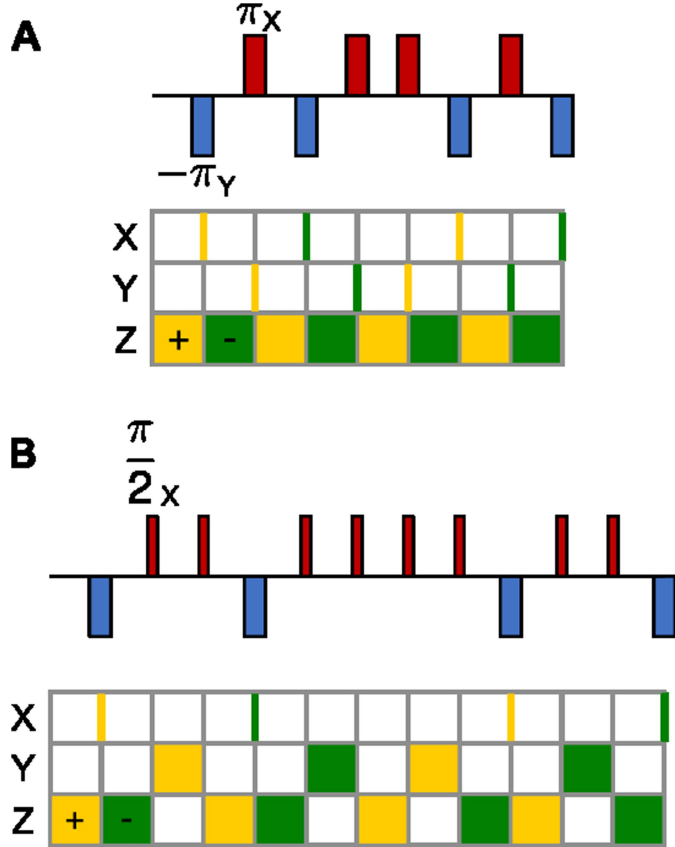
Supplementary information The online version contains supplementary material available at <https://doi.org/10.1038/s41586-024-07883-2>.

Correspondence and requests for materials should be addressed to Calder Miller or Jun Ye.

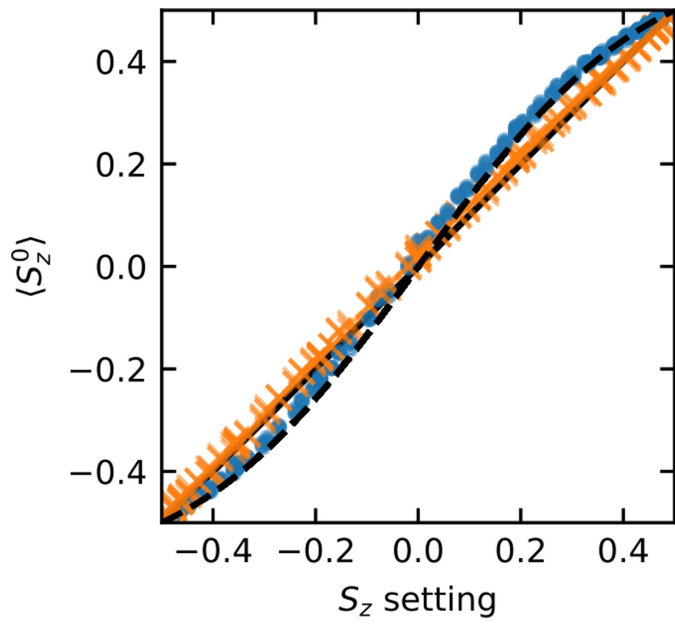
Peer review information *Nature* thanks the anonymous reviewers for their contribution to the peer review of this work. Peer reviewer reports are available.

Reprints and permissions information is available at <http://www.nature.com/reprints>.

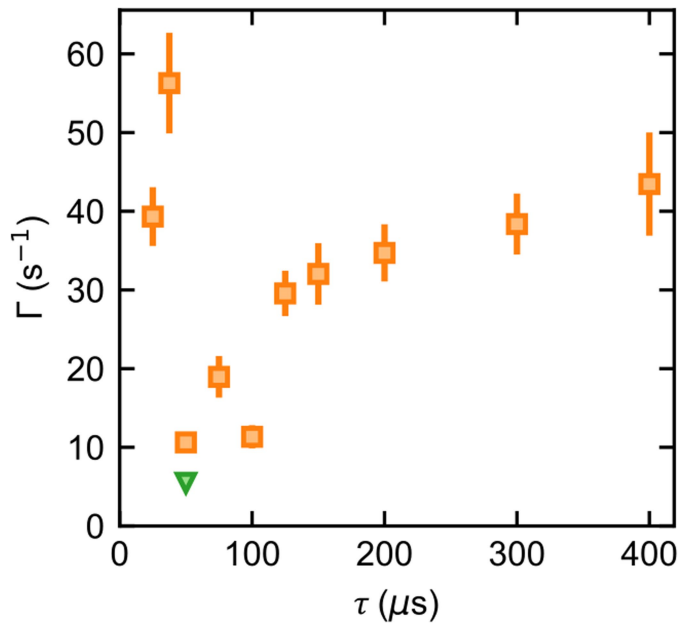
Article



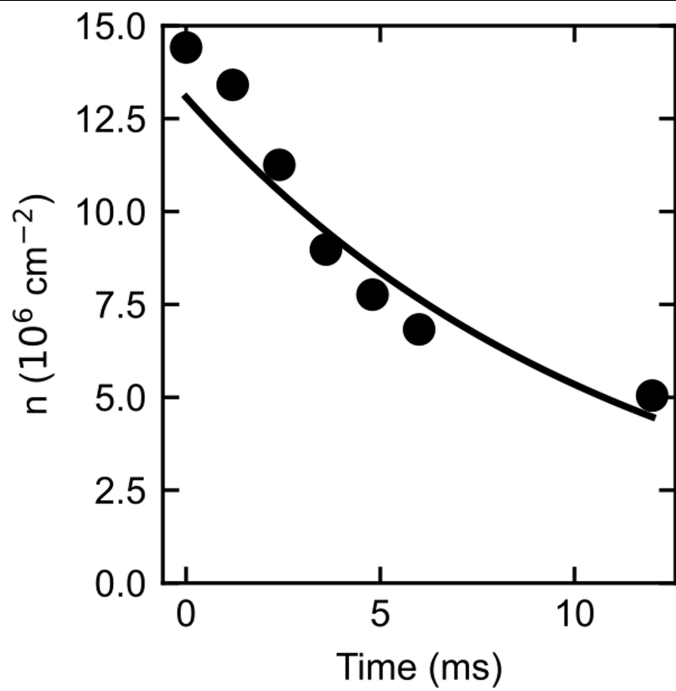
Extended Data Fig. 1 | Pulse sequences. Pulse sequences for generating OAT (XY8; **A**) and TAT (XY8-TAT; **B**) dynamics are shown using the notation of ref. 7. Narrow (wide) rectangles represent $\pi/2$ (π) pulses, red (blue) rectangles pulses about the $\pm X$ ($\pm Y$) axes, and pulses above (below) the line about the \pm ($-$) axes. The frame matrix representation shows which axis points along the $+Z$ direction as a function of time, with yellow (green) blocks representing axes originally along the \pm ($-$) directions.



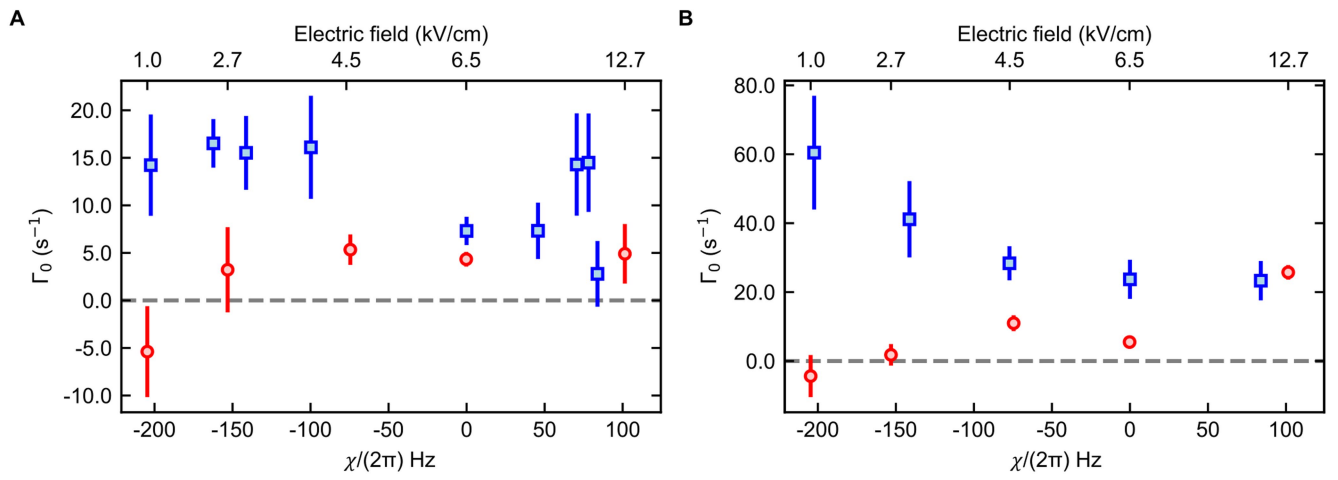
Extended Data Fig. 2 | Imaging correction. The measured value of $\langle S_z^0 \rangle$ is plotted (blue circles) as a function of the value prepared by a microwave pulse. The dashed curve is a fit to the loss model (see Methods). By inverting the model, the data can be corrected for loss during imaging (orange crosses).



Extended Data Fig. 3 | Optimizing Floquet pulse timing. The fitted contrast decay rate Γ is plotted as a function of pulse spacing τ for molecules with initial densities around $1.8(5) \times 10^7 \text{ cm}^{-2}$ in a 3D lattice with parameters set to produce the XXX model. The green triangle is the electric field-tuned data with a KDD pulse sequence and the orange squares are the Floquet data with a DROID-R2D2 pulse sequence. The error bars on the plot are 1 s.e. from stretched exponential fits.



Extended Data Fig. 4 | Number loss during TAT Floquet engineering. The average molecule density is plotted as a function of time as the XY8-TAT pulse sequence is repeatedly applied. The solid curve shows an exponential fit to the data, with time constant 11.2(6) ms.



Extended Data Fig. 5 | Single-particle contrast decay rates. The single-particle contrast decay rate Γ_0 is plotted as a function of χ electric field for electric field data (red circles and top axis) and Floquet data (blue squares)

for (A) molecules pinned in a deep 3D lattice and (B) itinerant molecules in a 1D lattice. The error bars are 1 s.e. from a linear fit.